



Four-channels reservoir computing based on polarization dynamics in mutually coupled VCSELs system

XING XING GUO,¹ SHUI YING XIANG,^{1,2,*} YA HUI ZHANG,¹ LIN LIN,¹ AI JUN WEN,¹ AND YUE HAO²

¹State Key Laboratory of Integrated Service Networks, Xidian University, Xi'an 710071, China

²State Key Discipline Laboratory of Wide Bandgap Semiconductor Technology, School of Microelectronics, Xidian University, Xi'an 710071, China

*syxiang@xidian.edu.cn

Abstract: A novel Four-channels reservoir computing (RC) based on polarization dynamics in mutually coupled vertical cavity surface emitting lasers (MDC-VCSELs) is proposed and demonstrated numerically. Here, the four channels are realized in two orthogonal polarization modes (x-polarization and y-polarization modes) of two VCSELs for the first time. A chaotic time series prediction task is employed to quantitatively evaluate the prediction performance of the proposed system. It is found that the Four-channels RC based on MDC-VCSELs can produce comparable prediction performance with One-channel RC, and it is possible to increase four times information processing rate by using the Four-channels RC. Besides, the effects of injection current, external injection strength, frequency detuning, coupling strength, as well as internal parameters on the prediction performance of the Four-channels RC based on MDC-VCSELs are carefully examined. Moreover, the influences of sampled period of input signal and the number of virtual nodes are also considered. The proposed Four-channels RC based on MDC-VCSELs is valuable for further enhancing the information processing rate of RC-based neuromorphic photonic systems.

© 2019 Optical Society of America under the terms of the [OSA Open Access Publishing Agreement](#)

1. Introduction

Reservoir computing (RC) as a brain-inspired computational paradigm originated from recurrent neural network has been investigated theoretically and experimentally [1–10]. RC has been successfully applied in solving computationally hard tasks, such as speech recognition systems [3–6], financial forecasting [7], handwritten digit recognition [8,9], and chaotic systems prediction [10]. In a RC system, sequential input is nonlinearly mapped to a high dimensional space. Connection weights between input and node in the reservoir are fixed. Then the input-driven dynamic responses of all nodes in the reservoir are weighted and combined by the linear readout function of the output layer. Hence, only output weights need to be trained using simple algorithm, such as linear regression [11]. Usually, in the experimental implementation of a RC, a large number of randomly connected physical nodes are used as a standard reservoir to provide a sufficiently high dimensionality [11–13].

Recently, a simplified reservoir structure consisting of a single nonlinear node subject to delayed feedback was proposed by Appltant *et al.* [5]. After that, the delay-based RC has been implemented in optoelectronic [14,15], all-optical [6,16], and laser dynamical systems [17–25]. Among them, the laser dynamical system is a promising candidate to realize delay-based RC with ultra-high information processing rate, because of its inherently fast operation, parallelism, high bandwidth and ultra-low consumption. For example, in 2013, Brunner *et al.* experimentally demonstrated a semiconductor laser (SL) with delayed feedback as a reservoir. The transient responses of SL were employed for realizing RC with low classification and prediction error rates, and the information processing rate was up to 1 Gbps

[17]. In 2017, Romain *et al.* experimentally and numerically demonstrated a RC system based on an optically pumped laser with optical delayed feedback. In this system, the input signal was directly coupled to the optical delayed feedback beam without additional external injection [18]. In 2019, they further proposed a RC system based on a single quantum cascade laser (QCL). It was found that, even without external injection, the QCL subject to delayed optical feedback could extend stable parameter area contributing to good RC performances [24].

In these delay-based RC systems, it is easy to achieve a large number of virtual nodes by using time multiplexing [5]. The information processing rate in the delay-based RC associates with the number of virtual nodes. A small number of the virtual nodes is required for increasing the information processing rate when interval between the adjacent virtual nodes is fixed. Note that, to ensure good performance of the delay-based RC, more variability of virtual node state is desired for a RC system with a small number of the virtual nodes. However, previous investigations of the delay-based RC using laser dynamical systems have mainly concentrated on a single nonlinear node, the variability of virtual node state is limited [17–24]. Therefore, the information processing rate of the delay-based RC is also limited.

Lately, a new delay-based RC architecture consisting of several nonlinear nodes is proposed to solve problems more efficiently [25–27]. Interestingly, a single vertical cavity surface emitting laser (VCSEL) has been successfully employed to realize RC with enhanced computation performance [23]. It is well known that VCSEL is a popular candidate for various potential applications, such as optical computation, optical communication, and optical signal processing [28,29]. VCSEL exhibits many advantages, including high energy efficiency, low manufacturing cost, easy to integrate into 2D arrays [28,29]. In particular, two orthogonal polarization modes, x-polarization(XP) and y-polarization(YP) modes, may coexist in a VCSEL, and much richer polarization dynamics can be achieved in a mutually delay coupled (MDC) VCSELs system [30–35]. However, it is still open to explore the multi-channels RC based on MDC-VCSELs, particularly the effects of the polarization dynamics of MDC-VCSELs on the RC performance.

In this paper, a novel Four-channels RC system based on polarization dynamics in MDC-VCSELs is proposed and demonstrated numerically. The four channels are realized in two orthogonal polarization modes of two VCSELs for the first time. A Santa-Fe chaotic time series prediction task is utilized to evaluate our system. For the purpose of comparison, One-channel RC system based on MDC-VCSELs is also considered. The remainder of this paper is structured as follows. In Section 2, the system design and operation principle diagram of Four-channels RC system based on MDC-VCSELs, the rate equation model and the task are introduced in detail. In Section 3, by numerical bifurcation analysis, the polarization dynamical states and stable regions of MDC-VCSELs are identified. Then the prediction performance has been examined and compared for both the Four-channels RC and the One-channel RC systems. The influences of injection current, external injection strength, frequency detuning, coupling strength, as well as internal parameters on the prediction performance of Four-channels RC based on MDC-VCSELs are also taken into account. Moreover, the roles of sampled period of input signal, and the number of virtual nodes are also considered. Finally, the conclusions are given in Section 4.

2. System model

2.1 System design and operation principle diagram

Here, the system design and operation principle diagram of the proposed Four-channels RC system based on MDC-VCSELs is shown in Fig. 1. Two VCSELs with four channels are used as a reservoir. The four channels are realized in two orthogonal polarization modes of the two VCSELs. The number of virtual nodes of each channel is Z , and the total number of virtual nodes is $M = 4Z$. The interval between the adjacent virtual nodes is θ . The sampled

period of input signal is $T = Z\theta$, and the information processing rate is $R_4 = 1/T$. It can be seen that, four inputs $S_{1x,1y,2x,2y}$ are coupled to the XP and YP modes of VCSEL1 and VCSEL2 through four Mach-Zehnder modulators (MZMs), respectively. The XP and YP modes of VCSEL1 (VCSEL2) are injected to the XP and YP modes of VCSEL2 (VCSEL1) in parallel. Finally, four transient responses $E_{1x,2x,1y,2y}$ from each of the four channels are extracted for post-processing, respectively. We only consider one input signal under four random binary masks $(-1, 1)$, leading to four different transient responses. Thus, as shown in Fig. 2, in the post-processing phase, the virtual node states extracted from the four channels are put into four matrices V_{12x} , V_{12y} , V_{21x} and V_{21y} , respectively. Then the four matrices are merged into one matrix V for post-processing, which can lead to more abundant transient responses than that of a single matrix. For One-channel RC, we only set one masked input signal, and only one matrix V_{12x} is employed for post-processing.

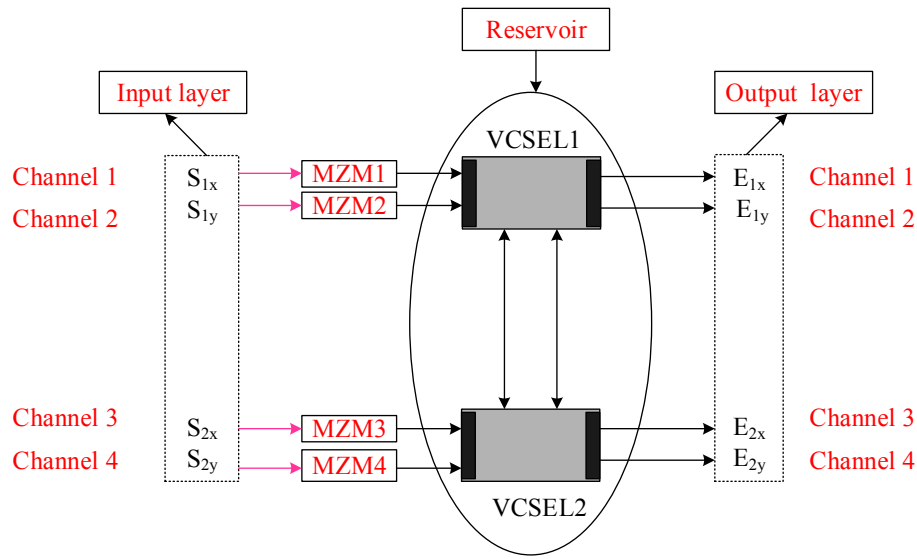


Fig. 1. System design and operation principle diagram of the Four-channels RC based on MDC-VCSELs with three layers: input layer, reservoir and output layer. VCSEL: vertical cavity surface emitting laser, MZMs: Mach-Zehnder modulators, the pink lines indicate the electric path and the black lines represent the optical path.

$$\begin{array}{cccc}
 V_{12x} & V_{12y} & V_{21x} & V_{21y} \\
 \begin{bmatrix} 1x_{11} & 1x_{12} & \cdots & 1x_{1m} \\ 1x_{21} & 1x_{22} & \cdots & 1x_{2m} \\ \vdots & \vdots & \ddots & \vdots \\ 1x_{j1} & 1x_{j2} & \cdots & 1x_{jm} \end{bmatrix} & \begin{bmatrix} 1y_{11} & 1y_{12} & \cdots & 1y_{1m} \\ 1y_{21} & 1y_{22} & \cdots & 1y_{2m} \\ \vdots & \vdots & \ddots & \vdots \\ 1y_{j1} & 1y_{j2} & \cdots & 1y_{jm} \end{bmatrix} & \begin{bmatrix} 2x_{11} & 2x_{12} & \cdots & 2x_{1m} \\ 2x_{21} & 2x_{22} & \cdots & 2x_{2m} \\ \vdots & \vdots & \ddots & \vdots \\ 2x_{j1} & 2x_{j2} & \cdots & 2x_{jm} \end{bmatrix} & \begin{bmatrix} 2y_{11} & 2y_{12} & \cdots & 2y_{1m} \\ 2y_{21} & 2y_{22} & \cdots & 2y_{2m} \\ \vdots & \vdots & \ddots & \vdots \\ 2y_{j1} & 2y_{j2} & \cdots & 2y_{jm} \end{bmatrix} \\
 \vdots & \vdots & \vdots & \vdots \\
 V & \left[V_{12x}, V_{12y}, V_{21x}, V_{21y} \right]
 \end{array}$$

Fig. 2. The virtual node states matrix for each channel.

2.2 Rate equation model

In this paper, the MDC-VCSELs system with parallel polarization injection is considered. The rate equations are derived based on the well-known spin-flip model [36,37]. The slowly varied complex field amplitudes of XP and YP modes are $E_{1x,2x}$ and $E_{1y,2y}$. The difference between carrier inversions with opposite spins are $n_{1,2}$, and the total population inversions are $N_{1,2}$. The modified rate equations incorporating the mutual coupling and external injections are described as follows [36,37]:

$$\frac{dE_{1x}}{dt} = \kappa(1+i\alpha)(N_1E_{1x} - E_{1x} + in_1E_{1y}) - (\gamma_a + i\gamma_p)E_{1x} + k_{21x}E_{2x}(t - \tau_{21})e^{-i\omega_2\tau_{21}}e^{i\Delta\omega_{21}t} + k_{inj1x}\mathcal{E}_{1x}(t) + F_{1x} \quad (1)$$

$$\frac{dE_{1y}}{dt} = \kappa(1+i\alpha)(N_1E_{1y} - E_{1y} - in_1E_{1x}) + (\gamma_a + i\gamma_p)E_{1y} + k_{21y}E_{2y}(t - \tau_{21})e^{-i\omega_2\tau_{21}}e^{i\Delta\omega_{21}t} + k_{inj1y}\mathcal{E}_{1y}(t) + F_{1y} \quad (2)$$

$$\frac{dE_{2x}}{dt} = \kappa(1+i\alpha)(N_2E_{2x} - E_{2x} + in_2E_{2y}) - (\gamma_a + i\gamma_p)E_{2x} + k_{12x}E_{1x}(t - \tau_{12})e^{-i\omega_1\tau_{12}}e^{i\Delta\omega_{12}t} + k_{inj2x}\mathcal{E}_{2x}(t) + F_{2x} \quad (3)$$

$$\frac{dE_{2y}}{dt} = \kappa(1+i\alpha)(N_2E_{2y} - E_{2y} - in_2E_{2x}) + (\gamma_a + i\gamma_p)E_{2y} + k_{21y}E_{1y}(t - \tau_{12})e^{-i\omega_1\tau_{12}}e^{i\Delta\omega_{12}t} + k_{inj2y}\mathcal{E}_{2y}(t) + F_{2y} \quad (4)$$

$$\frac{dn_{1,2}}{dt} = -\gamma_s n_{1,2} - \gamma_N [n_{1,2}(|E_{1x,2x}|^2 + |E_{1y,2y}|^2) + iN_{1,2}(E_{1y,2y}E_{1x,2x}^* - E_{1x,2x}E_{1y,2y}^*)] \quad (5)$$

$$\frac{dN_{1,2}}{dt} = \gamma_N [\mu_{1,2} - N_{1,2}(1 + |E_{1x,2x}|^2 + |E_{1y,2y}|^2) + in_{1,2}(E_{1x,2x}E_{1y,2y}^* - E_{1y,2y}E_{1x,2x}^*)] \quad (6)$$

where the subscripts 1 and 2 in Eqs. (1)-(6) denote VCSEL1 and VCSEL2, respectively. κ represents the field decay rate. α is the linewidth enhancement factor. γ_s is the spin-flip rate, and γ_N indicates the decay rate of N . γ_a (γ_p) expresses the linear dichroism (linear birefringence). $\mu_1 = \mu_2 = \mu$ is the normalized injection current, while $\mu = 1$ implies at the threshold. The third term in Eqs. (1)-(3) represents an injection from the XP mode of VCSEL2 (VCSEL1) into XP mode of VCSEL1 (VCSEL2). Similarly, the third term in Eqs. (2)-(4) denotes an injection from the YP mode of VCSEL2 (VCSEL1) into YP mode of VCSEL1 (VCSEL2). The corresponding coupling strengths are k_{21x} , k_{12x} , k_{21y} and k_{12y} . τ_{12} (τ_{21}) is the coupling delay between the two VCSELs. For simplicity, we assume $k_{21x} = k_{21y} = k_{12x} = k_{12y} = k_r$ and $\tau_{12} = \tau_{21} = \tau$. ω_1 (ω_2) denotes the center frequency of two orthogonal polarization outputs of VCSEL1 (VCSEL2). The difference of angular frequency is defined as $\Delta\omega_{21} = \omega_2 - \omega_1$ ($\Delta\omega_{12} = \omega_1 - \omega_2$), and $\Delta\omega_{21} = 2\pi\Delta f_{21}$ ($\Delta\omega_{12} = 2\pi\Delta f_{12}$). Δf_{21} (Δf_{12}) indicates the center frequency detuning between two VCSELs. The last term in Eqs. (1)-(4)

means the external injection. Four masked input signals ($s_{1x}, s_{1y}, s_{2x}, s_{2y}$) modulated through four MZMs are injected into the four channels, respectively. k_{inj1x} ($k_{inj1y}, k_{inj2x}, k_{inj2y}$) is the external injection strength with $k_{inj1x} = k_{inj1y} = k_{inj2x} = k_{inj2y} = k_{inj}$. Here, the outputs of the MZMs $\varepsilon_{1x,1y,2x,2y}(t)$ are described as [38]:

$$\varepsilon_{1x,1y,2x,2y}(t) = \frac{|\varepsilon_0|}{2} e^{i\Delta\omega_{x,1y,2x,2y}t} \{1 + e^{i[s_{1x,1y,2x,2y}(t) + \Phi_0]}\}, \quad (7)$$

where Φ_0 ($|\varepsilon_0|$) is the bias voltage of the MZMs (the injection field amplitude). $\Delta\omega_x = 2\pi\Delta f_{1x}$ ($\Delta\omega_y = 2\pi\Delta f_{1y}$) is the angular frequency detuning between the XP (YP) mode of VCSEL1 and the injected field. Δf_{1x} (Δf_{1y}) is the frequency detuning between the XP (YP) mode of VCSEL1 and the injected field. $\Delta\omega_x = 2\pi\Delta f_{2x}$ ($\Delta\omega_y = 2\pi\Delta f_{2y}$) is the angular frequency detuning between the XP (YP) mode of VCSEL2 and the injected field. Δf_{2x} (Δf_{2y}) is the frequency detuning between the XP (YP) mode of VCSEL2 and the injected field. For simplicity, we set $\Delta f_{1x} = \Delta f_{1y} = \Delta f_{2x} = \Delta f_{2y} = \Delta f$. The spontaneous emission noises for the two VCSELs modeled by Langevin sources are $F_{1x,2x} = \sqrt{\beta/2}(\sqrt{N_{1,2} + n_{1,2}}\xi^a + \sqrt{N_{1,2} - n_{1,2}}\xi^b)$ and $F_{1y,2y} = -i\sqrt{\beta/2}(\sqrt{N_{1,2} + n_{1,2}}\xi^b - \sqrt{N_{1,2} - n_{1,2}}\xi^a)$ [32], respectively. β is the strength of the spontaneous emission. ξ^a (ξ^b) is independent Gaussian white noises sources with unit variance and zero mean. The above rate equations are numerically solved by a second-order Runge-Kutta method with a time step of $\Delta t = 2\text{ps}$ [38].

2.3 Santa-Fe chaotic time series prediction task

We employ the Santa-Fe chaotic time series prediction task as a benchmark test to evaluate the prediction performance of Four-channels RC system based on MDC-VCSELs. The goal for the task is to predict the next step of the chaotic time series gained from a far-infrared laser experimentally [39]. The first 3000 points in the Santa-Fe data set are used for training and the next 1000 are adopted for testing. The normalized mean square error ($NMSE$) is defined to quantitatively evaluate the prediction performance of this benchmark task [38]:

$$NMSE = \frac{\langle \|Y(L) - \bar{Y}(L)\|^2 \rangle}{\sigma^2} \quad (8)$$

where $\bar{Y}(L)$ is the target value and $Y(L)$ is the predicted value, $\langle \bullet \rangle$ and $\|\bullet\|$ represent the average and the norm, respectively. L is the discrete time index, and σ represents standard deviation. Generally, when $NMSE \leq 0.1$, the prediction performance is considered to be good [38]. Note that the training-test process is repeated ten times to obtain the final values.

3. Numerical results

In this section, the prediction performance of Four-channels RC based on MDC-VCSELs is evaluated quantitatively in detail. For the purpose of comparison, we also consider the One-channel RC based on MDC-VCSELs. At first, the polarization dynamical states and stable regions of MDC-VCSELs are analyzed and identified. Then, we study the influences of injection current, external injection strength, frequency detuning, coupling strength, and internal parameters on the prediction performance of Four-channels RC based on MDC-VCSELs. Moreover, the roles of sampled period of input signal, and the number of virtual

nodes are also considered. In our simulation, the following parameter values are adopted: $\alpha = 3$, $\kappa = 300\text{ns}^{-1}$, $\gamma_a = 0.1\text{ns}^{-1}$, $\gamma_p = 10\text{ns}^{-1}$, $\gamma_N = 1\text{ns}^{-1}$, $\gamma_s = 50\text{ns}^{-1}$, $\mu = 1.01$, $\omega_1 = 2\pi c / \lambda$ and $\omega_2 = \omega_1 - 2\pi\Delta f_{12}$ with $\lambda = 850\text{nm}$, $k_r = 10\text{ns}^{-1}$, $k_{inj} = 30\text{ns}^{-1}$, $\Delta f_{12,21} = 0\text{GHz}$, $\tau = 0.5\text{ns}$, $\beta = 1 \times 10^{-6}$, $|\epsilon_0| = 1$, $\Phi_0 = 0$, $\Delta f = 0\text{GHz}$, $\theta = 25\text{ps}$, $Z = 20$, $M = 80$ [21,22,31]. Note that those parameters are fixed, unless otherwise noted.

To begin with, the polarization-resolved intensities as a function of the normalized injection current μ for free-running VCSEL is shown in Fig. 3. Here, the mean intensities are calculated as $\langle I_{x,y} \rangle = \langle |E_{x,y}(t)|^2 \rangle$ for the XP and YP modes. As can be seen, when $1 < \mu \leq 1.55$, the XP mode is the dominant polarization mode while the YP mode is suppressed completely. When $\mu > 1.55$, the YP mode starts to oscillate. As the injection current continues to increase, the polarization-resolved intensities of both modes increase. However, the XP mode is still the dominant polarization mode.

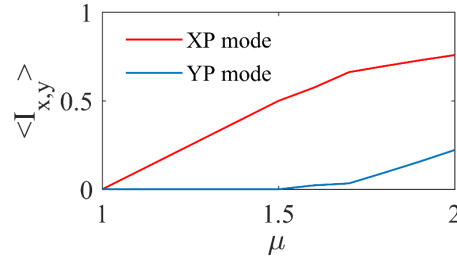


Fig. 3. The polarization-resolved intensities as a function of the normalized injection current μ for free-running VCSEL.

The bifurcation diagrams as a function of the normalized injection current μ are also shown in Fig. 4. Here, we set $s_{1x} = s_{1y} = s_{2x} = s_{2y} = 0$ and $k_{inj} \neq 0$. $I_{x,y} = |E_{x,y}(t)|^2$ are the intensities of XP and YP modes. It can be seen that the two VCSELs exhibit similar dynamical state and two orthogonal polarization modes coexist. More precisely, when $\mu \leq 1.47$, XP and YP modes of both VCSELs remain stable due to injection locking effect. As μ gradually increases, for XP mode, it can be seen from Figs. 4(a1) and (a2), the outputs of the two VCSELs oscillate with multiple periods resulting in several branches in the bifurcation diagrams. For YP mode, as can be seen from Figs. 4(b1) and (b2), the outputs of the two VCSELs oscillate periodically resulting in two branches. Note that, these stable regions are associated with the good performance of a RC system [5].

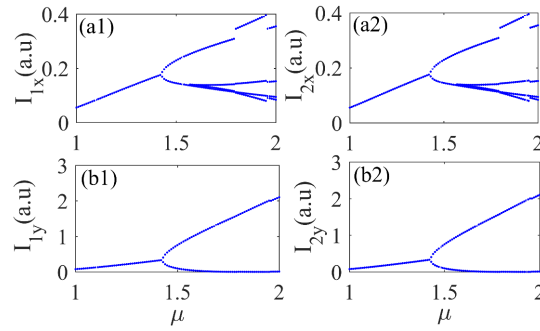


Fig. 4. Numerical bifurcation diagrams as a function of μ for (the first column) VCSEL1 and (the second column) VCSEL2, for (a1, a2) XP mode, for (b1, b2) YP mode, with $k_r=10\text{ns}^{-1}$ and $k_{inj}=30\text{ns}^{-1}$.

Next, the *NMSE* values for Four-channels RC and One-channel RC based on MDC-VCSELs as a function of normalized injection current μ are shown in Fig. 5. Here, virtual node interval is fixed at $\theta = 25\text{ps}$. For Four-channels RC based on MDC-VCSELs, the number of virtual nodes of each channel is $Z = 20$, and the total number of virtual nodes is $M = 4Z = 80$. Thus, the information processing rate is $R_4 = 1/(Z\theta) = 2\text{Gbps}$. For comparison, for One-channel RC ($k_{inj21x} = k_{inj21y} = k_{inj1x} = k_{inj1y} \neq 0$, $s_{21x} \neq 0$ and $s_{21y} = s_{12x} = s_{12y} = 0$), the number of virtual nodes of one channel is set as $Z = 80$ corresponding to $R_1 = 1/(Z\theta) = 0.5\text{Gbps}$. That is to say, the information processing rate for Four-channels RC based on MDC-VCSELs is four times higher than that for One-channel RC. As can be seen that, the *NMSE* curves for Four-channels RC and One-channel RC are almost overlapped for $\mu \leq 1.45$. Then the *NMSE* values of Four-channels RC (One-channel RC) based on MDC-VCSELs increase significantly for $\mu > 1.45$ ($\mu > 1.52$), because of the onset of instabilities, which is in agreement with the experimental result in [40]. Besides, a good prediction performance of Four-channels RC (One-channel RC) based on MDC-VCSELs can be obtained when $\mu \leq 1.9$ ($\mu \leq 1.55$). Hence, compared with the One-channel RC based on MDC-VCSELs, the Four-channels RC based on MDC-VCSELs can produce comparable prediction performance with much faster information processing rate.

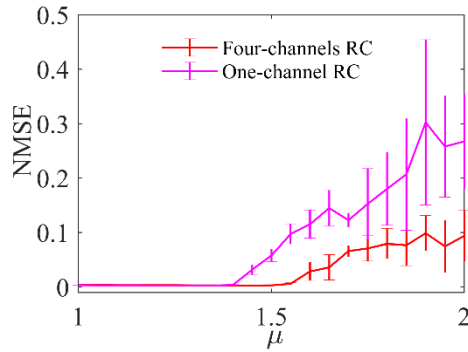


Fig. 5. The *NMSE* values of RC system based on MDC-VCSELs as a function of μ for Four-channels RC with $Z = 20$ and $R_4 = 2\text{Gbps}$, for One-channel RC with $Z = 80$ and $R_1 = 0.5\text{Gbps}$, with $k_r=10\text{ns}^{-1}$ and $k_{inj}=30\text{ns}^{-1}$.

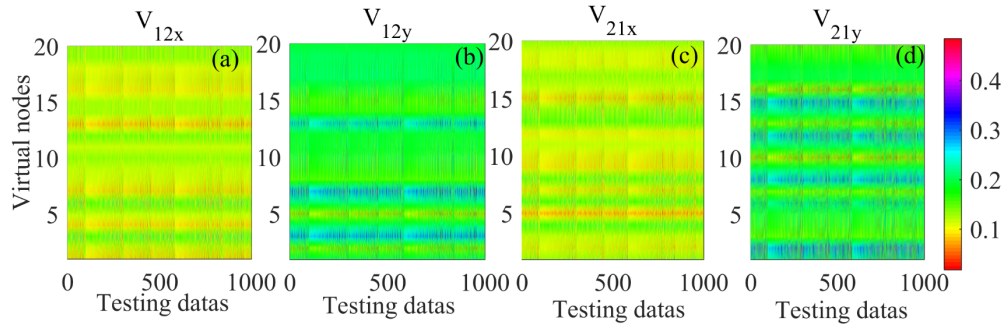


Fig. 6. The transient responses of the XP and YP modes of Four-channels RC based on MDC-VCSELs, with $k_{inj} = 30\text{ns}^{-1}$, $k_d = 10\text{ns}^{-1}$ and $\mu = 1.2$.

In the following, we only focus on Four-channels RC based on MDC-VCSELs. At first, we consider the transient responses of the XP and YP modes of Four-channels RC based on MDC-VCSELs. Here, we set $k_{inj} = 30\text{ns}^{-1}$, $k_d = 10\text{ns}^{-1}$ and $\mu = 1.2$. When 1000 testing data are injected into the Four-channels RC system, the spatio-temporal plots for the four matrices V_{12x} , V_{12y} , V_{21x} and V_{21y} are shown in Fig. 6, respectively. The transient responses for input signals are represented by column-shaped patterns throughout the entire spatio-temporal plot. It is indicated that rich information has been preserved.

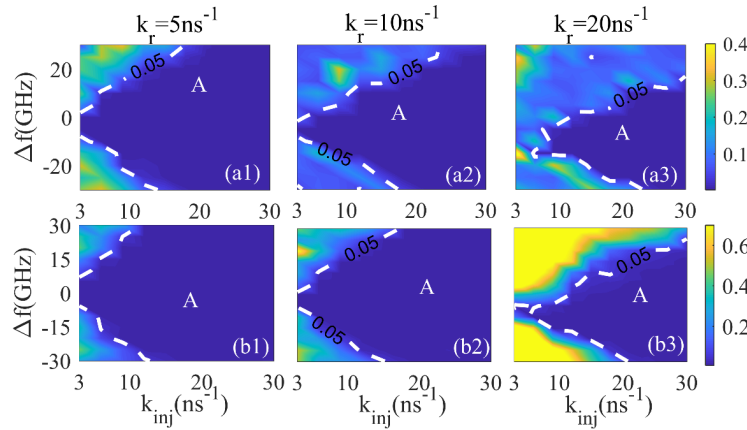


Fig. 7. Two dimensional maps of the $NMSE$ values of Four-channels RC system based on MDC-VCSELs in the parameter space of Δf and k_{inj} , with $\mu = 1.01$. (a1, a2, a3) for $k_r = 5\text{ns}^{-1}$, $k_r = 10\text{ns}^{-1}$, $k_r = 20\text{ns}^{-1}$ with $\Delta f_{12} = 0\text{GHz}$; (b1, b2, b3) for $k_r = 5\text{ns}^{-1}$, $k_r = 10\text{ns}^{-1}$, $k_r = 20\text{ns}^{-1}$ with $\Delta f_{12} = 5\text{GHz}$.

To obtain the dependence of the prediction performance, the two-dimensional maps of $NMSE$ values in the parameter space of external injection strength k_{inj} and frequency detuning Δf are presented for different k_r and Δf_{12} in Fig. 7. Here, Δf_{12} is fixed at 0 for Figs. 7(a1)-(a3). A better prediction performance region with $NMSE \leq 0.05$, is denoted as region A by the contour lines. As shown in Fig. 7(a1), for $k_r = 5\text{ns}^{-1}$, the region A mainly locates at larger k_{inj} for all the considered Δf , which is similar to the injection locking area in [41]. That is to say, the good performance of RC is closely related to the injection locking

effect. For $k_r = 10\text{ns}^{-1}$ as shown in Fig. 7(a2), regions A becomes narrow. For larger coupling strength $k_r = 20\text{ns}^{-1}$ as shown in Fig. 7(a3), regions A becomes even narrower. Besides, higher k_r leads to the shift of the region A toward negative Δf . It is indicated that a larger k_{inj} , smaller k_r and negative Δf are desired for better prediction performance. Without loss of generality, we also consider other cases of Δf_{12} , and obtain similar results. A representative case for $\Delta f_{12} = 5\text{GHz}$ is shown Figs. 7(b1)-(b3). It can be seen that good prediction performance of Four-channels RC based on MDC-VCSELs can be also obtained.

Then two dimensional maps of $NMSE$ values in the parameter space of k_r and k_{inj} are further presented in Fig. 8 for different Δf . It is found that, a larger Δf leads to a narrower region A. Besides, for a relatively large Δf , the region A mainly covers the range with $k_{inj} > k_r$, which is also attributed to the injection locking effect.

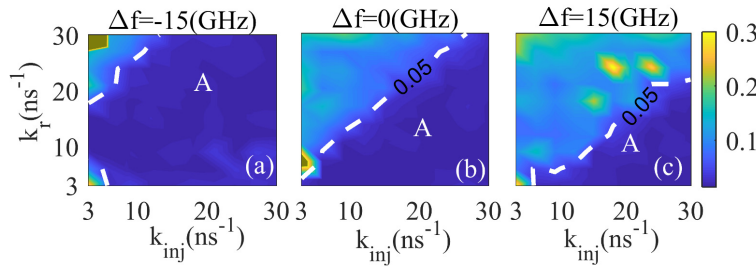


Fig. 8. Two dimensional maps of the $NMSE$ values of Four-channels RC system based on MDC-VCSELs in the parameter space of k_r and k_{inj} , with $\mu = 1.01$ and $\Delta f_{12} = 0$. (a) for $\Delta f = -15\text{GHz}$, (b) for $\Delta f = 0\text{GHz}$, (c) $\Delta f = 15\text{GHz}$.

Subsequently, the $NMSE$ values as a function of coupling strength k_r for different k_{inj} and three cases of μ are shown in Fig. 9. Here, Δf and Δf_{12} are fixed at 0GHz , and k_r is varied from 0ns^{-1} to 30ns^{-1} . For $\mu = 1.01$, as can be observed from Fig. 9(a) and inset, for $k_{inj} = 10\text{ns}^{-1}$, the $NMSE$ values decrease with k_r firstly when $0\text{ns}^{-1} \leq k_r \leq 14\text{ns}^{-1}$, and then increase with the further increment of k_r . Similar results can be obtained for $k_{inj} = 15\text{ns}^{-1}$ and $k_{inj} = 20\text{ns}^{-1}$. Obviously, a wider range of k_r contributing to $NMSE \leq 0.001$ can be obtained for a larger k_{inj} . It is indicated that, a larger k_{inj} contributes to better prediction performance of Four-channels RC based on MDC-VCSELs. For $\mu = 1.2$, similar trends are obtained in Fig. 9(b). But for a given k_{inj} , the maximum k_r leading to $NMSE \leq 0.001$ is smaller than that for the case of $\mu = 1.01$. Besides, when in the range of k_r contributing to $NMSE < 0.01$ for the case of $\mu = 1.2$, the fluctuation of the error bars of the $NMSE$ becomes larger compared to the case of $\mu = 1.01$. This may be because that an injection current that is close to the threshold current makes the RC system based on MDC-VCSELs more stable [40]. For a much larger μ , such as $\mu = 1.5$, as can be seen from Fig. 9(c), for $k_{inj} = 10\text{ns}^{-1}$, the values of $NMSE$ are basically greater than 0.1 for all the considered k_r . However, for some larger k_{inj} , such as $k_{inj} = 20\text{ns}^{-1}$, $k_{inj} = 25\text{ns}^{-1}$, and $k_{inj} = 30\text{ns}^{-1}$, similar results to the trend for the

cases of $\mu = 1.01$ and $\mu = 1.2$ can be obtained. Besides, with the growth of k_{inj} , the maximum k_r leading to $NMSE \leq 0.001$ increases. That is to say, increasing k_{inj} can improve the performance of Four-channels RC system when using larger currents.

The effects of internal parameters on the prediction performance of Four-channels RC based on MDC-VCSELs are also considered. Figure 10(a) shows the variation of $NMSE$ values with the coupling strength k_r under some typical values of the linear dichroism γ_a . It can be seen that, for all the considered γ_a , the prediction performance of Four-channels RC based on MDC-VCSELs is good and is hardly affected by the γ_a . Besides, the effect of linear birefringence γ_p on the prediction performance is also examined. The $NMSE$ curves are further shown in Fig. 10(b). It can be observed that the $NMSE$ curves are almost overlapped for different γ_p . That is to say, the prediction performance of Four-channels RC based on MDC-VCSELs is hardly affected by the internal parameters of VCSELs.

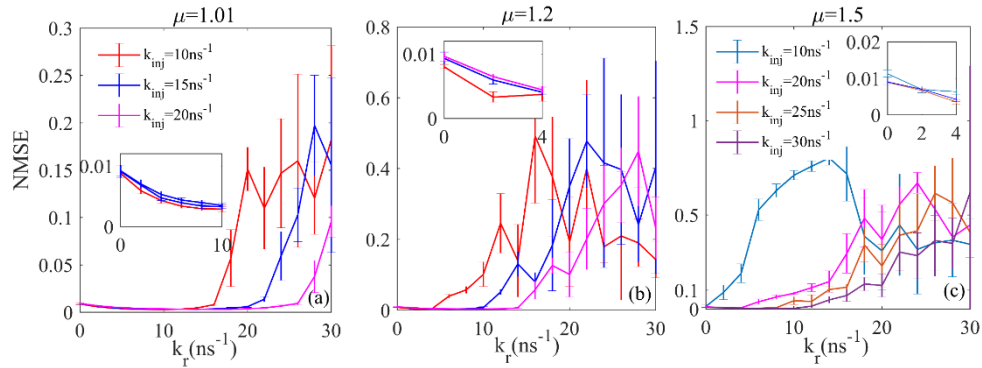


Fig. 9. The $NMSE$ values of Four-channels RC system based on MDC-VCSELs as a function of the k_r for different k_{inj} , with $\Delta f = 0$ and $\Delta f_{12} = 0$, (a) for $\mu = 1.01$, (b) for $\mu = 1.2$, (c) for $\mu = 1.5$.

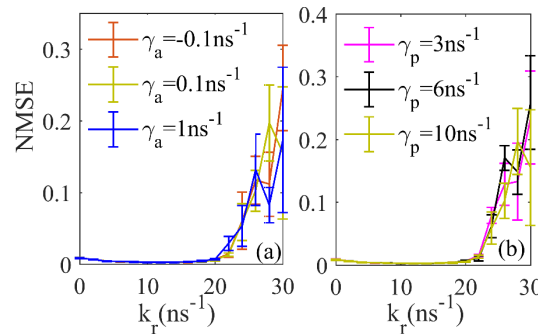


Fig. 10. The $NMSE$ values of Four-channels RC system based on MDC-VCSELs as a function of k_r for different internal parameters with $\mu = 1.01$, $k_{inj} = 30 \text{ ns}^{-1}$, $\Delta f_{12} = 0$, $\Delta f = 0$, (a) for $\gamma_a = -0.1 \text{ ns}^{-1}, 0.1 \text{ ns}^{-1}, 1 \text{ ns}^{-1}$, (b) for $\gamma_p = 3 \text{ ns}^{-1}, 6 \text{ ns}^{-1}, 10 \text{ ns}^{-1}$.

At last, to discuss the information processing rate of the proposed RC system, we further consider the influences of sampled period T for different virtual node interval θ in Fig. 11. Here, the coupling delay τ is also set as T . Note, as T is changed, the information

processing rate $R_4 = 1/T$ will also be varied. It can be seen from Fig. 11(a), for all the considered θ , $NMSE$ curves generally present a decrease trend with the increment of T . It is indicated that the prediction performance of Four-channels RC is improved with the growth of T . In addition, a smaller θ leads to a lower $NMSE$ for a given T . More precisely, for $\theta = 10\text{ps}$, it can be observed that $NMSE$ values are below 0.1 for $T \geq 0.05\text{ns}$. That is to say, the fastest information processing rate R_4 in our proposed RC system can be up to 20Gbps, which is much faster than the information processing rate reported in delay-based RC systems based on single nonlinear node [17–25]. Besides, for another case when the coupling delay τ is fixed at 0.5ns, it can be seen from Fig. 11(b), similar trends can be achieved. Even for a much larger τ , such as $\tau = 10\text{ns}$, as can be seen from Fig. 11(c), obviously, similar results also can be observed.

For the case of the mentioned highest information processing rate ($R_4 = 20\text{Gbps}$ obtained from Fig. 11(a)), the variation of $NMSE$ values with the number of virtual nodes of each channel Z is further shown in Fig. 12. Here, the sampled period $T = Z\theta = 0.05\text{ns}$, and $\tau = T$. It can be seen that, when $Z \leq 8$, $NMSE$ values firstly decrease drastically. Then with the further increment of Z , $NMSE$ values decrease slowly. Interestingly, the trend of $NMSE$ curve for Four-channels RC based on MDC-VCSELs is similar to that for the single channel RC system based on the conventional SLs [22].

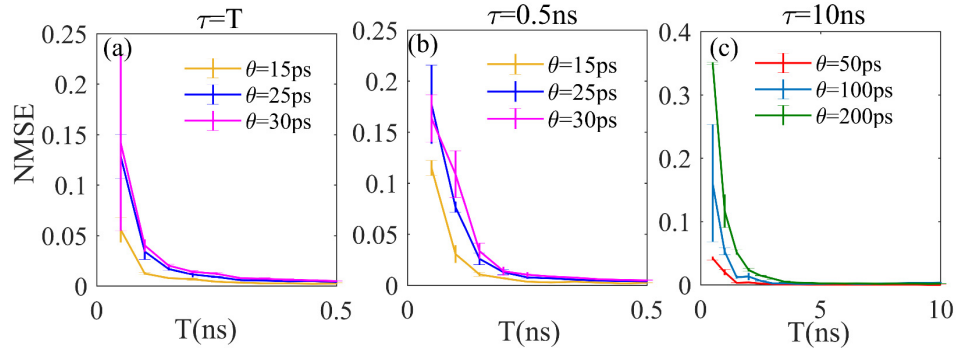


Fig. 11. The $NMSE$ values of Four-channels RC system based on MDC-VCSELs as a function of the T for different θ for (a) $\tau = T$, (b) $\tau = 0.5\text{ns}$, (c) $\tau = 10\text{ns}$, with $\mu = 1.01$, $k_{inj} = 30\text{ns}^{-1}$, $k_r = 10\text{ns}^{-1}$, $\Delta f_{12} = 0$, $\Delta f = 0$.

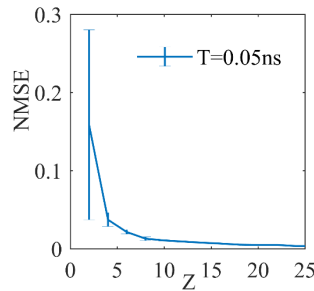


Fig. 12. The $NMSE$ values of Four-channels RC system based on MDC-VCSELs as a function of Z for $T = Z\theta = \tau = 0.05\text{ns}$ with $\mu = 1.01$, $k_{inj} = 30\text{ns}^{-1}$, $k_r = 10\text{ns}^{-1}$, $\Delta f_{12} = 0$, $\Delta f = 0$.

4. Conclusion

In summary, a Four-channels RC system based on polarization dynamics in mutually delay coupled VCSELs is proposed. The four channels are realized in two orthogonal polarization modes of two VCSELs for the first time. It is shown that, Four-channels RC based on MDC-VCSELs can produce comparable prediction performance with One-channel RC, and four times information processing rate can be achieved for Four-channels RC. The parameter regions leading to better prediction performance of Four-channels RC based on MDC-VCSELs are greatly broadened for smaller coupling strength, larger external injection strength and negative frequency detuning. Besides, the prediction performance is hardly affected by the internal parameters of VCSEL. Moreover, the fastest information processing rate in our proposed RC system can be even up to 20Gbps, which is much faster than the information processing rate reported in delay-based RC systems based on single nonlinear node. This work may be valuable for the realization of higher rate and multichannel RC.

Funding

National Postdoctoral Program for innovative Talents in China (BX201600118), National Natural Science Foundation of China (61674119), Young Talent fund of University Association for Science and Technology in Shaanxi, China (20160109), Natural Science Basic Research Plan in Shaanxi Province of China (2017JM6002).

Acknowledgments

This work was supported in part by the National Postdoctoral Program for innovative Talents in China (Grant BX201600118), the National Natural Science Foundation of China (Grants 61674119), the Young Talent fund of University Association for Science and Technology in Shaanxi, China (Grants 20160109), Natural Science Basic Research Plan in Shaanxi Province of China (Grants 2017JM6002).

References

1. H. Jaeger and H. Haas, "Harnessing nonlinearity: predicting chaotic systems and saving energy in wireless communication," *Science* **304**(5667), 78–80 (2004).
2. H. Jaeger, W. Maass, and J. Principe, "Special issue on echo state networks and liquid state machines," *Neural Netw.* **20**(3), 287–289 (2007).
3. D. Verstraeten, B. Schrauwen, D. Stroobandt, and J. Van Campenhout, "Isolated word recognition with the liquid state machine: a case study," *Inf. Process. Lett.* **95**(6), 521–528 (2005).
4. D. Verstraeten, B. Schrauwen, and D. Stroobandt, "Reservoir-based techniques for speech recognition," in *Proceedings of IJCNN06, International Joint Conference on Neural Networks*, ed. (Academic), 1050–1053 (2006).
5. L. Appeltant, M. C. Soriano, G. Van der Sande, J. Danckaert, S. Massar, J. Dambre, B. Schrauwen, C. R. Mirasso, and I. Fischer, "Information processing using a single dynamical node as complex system," *Nat. Commun.* **2**(1), 468 (2011).
6. Q. Vinckier, F. Duport, A. Smerieri, K. Vandoorne, P. Bienstman, M. Haelterman, and S. Massar, "High-performance photonic reservoir computer based on a coherently driven passive cavity," *Optica* **2**(5), 438–446 (2015).
7. M. Lukoševičius, H. Jaeger, and B. Schrauwen, "Reservoir computing trends," *Künstl. Intell* **26**(4), 365–371 (2012).
8. M. Lukoševičius and H. Jaeger, "Reservoir computing approaches to recurrent neural network training," *Comput. Sci. Rev.* **3**(3), 127–149 (2009).
9. C. Du, F. Cai, M. A. Zidan, W. Ma, S. H. Lee, and W. D. Lu, "Reservoir computing using dynamic memristors for temporal information processing," *Nat. Commun.* **8**(1), 2204 (2017).
10. J. Pathak, B. Hunt, M. Girvan, Z. Lu, and E. Ott, "Model-free prediction of large spatiotemporally chaotic systems from data: A reservoir computing approach," *Phys. Rev. Lett.* **120**(2), 024102 (2018).
11. D. Verstraeten, B. Schrauwen, M. D'Haene, and D. Stroobandt, "An experimental unification of reservoir computing methods," *Neural Netw.* **20**(3), 391–403 (2007).
12. K. Vandoorne, P. Mechet, T. Van Vaerenbergh, M. Fiers, G. Morthier, D. Verstraeten, B. Schrauwen, J. Dambre, and P. Bienstman, "Experimental demonstration of reservoir computing on a silicon photonics chip," *Nat. Commun.* **5**(1), 3541 (2014).

13. B. Schneider, J. Dambre, and P. Bienstman, "Using digital masks to enhance the bandwidth tolerance and improve the performance of on-chip reservoir computing systems," *IEEE Trans. Neural Netw. Learn. Syst.* **27**(12), 2748–2753 (2016).
14. Y. Paquot, F. Duport, A. Smerieri, J. Dambre, B. Schrauwen, M. Haelterman, and S. Massar, "Optoelectronic reservoir computing," *Sci. Rep.* **2**(1), 287 (2012).
15. M. C. Soriano, S. Ortín, D. Brunner, L. Larger, C. R. Mirasso, I. Fischer, and L. Pesquera, "Optoelectronic reservoir computing: tackling noise-induced performance degradation," *Opt. Express* **21**(1), 12–20 (2013).
16. A. Dejonckheere, F. Duport, A. Smerieri, L. Fang, J. L. Oudar, M. Haelterman, and S. Massar, "All-optical reservoir computer based on saturation of absorption," *Opt. Express* **22**(9), 10868–10881 (2014).
17. D. Brunner, M. C. Soriano, C. R. Mirasso, and I. Fischer, "Parallel photonic information processing at gigabyte per second data rates using transient states," *Nat. Commun.* **4**(1), 1364 (2013).
18. R. M. Nguimdo, E. Lacot, O. Jacquin, O. Hugon, G. Van der Sande, and H. Guillet de Chatellus, "Prediction performance of reservoir computing systems based on a diode-pumped erbium-doped microchip laser subject to optical feedback," *Opt. Lett.* **42**(3), 375–378 (2017).
19. J. Nakayama, K. Kanno, and A. Uchida, "Laser dynamical reservoir computing with consistency: an approach of a chaos mask signal," *Opt. Express* **24**(8), 8679–8692 (2016).
20. J. Bueno, D. Brunner, M. C. Soriano, and I. Fischer, "Conditions for reservoir computing performance using semiconductor lasers with delayed optical feedback," *Opt. Express* **25**(3), 2401–2412 (2017).
21. R. M. Nguimdo, E. Lacot, O. Jacquin, O. Hugon, G. Van der Sande, and H. Guillet de Chatellus, "Prediction performance of reservoir computing systems based on a diode-pumped erbium-doped microchip laser subject to optical feedback," *Opt. Lett.* **42**(3), 375–378 (2017).
22. Y. Hou, G. Xia, W. Yang, D. Wang, E. Jayaprasath, Z. Jiang, C. Hu, and Z. Wu, "Prediction performance of reservoir computing system based on a semiconductor laser subject to double optical feedback and optical injection," *Opt. Express* **26**(8), 10211–10219 (2018).
23. J. Vatin, D. Rontani, and M. Sciamanna, "Enhanced performance of a reservoir computer using polarization dynamics in VCSELs," *Opt. Lett.* **43**(18), 4497–4500 (2018).
24. R. M. Nguimdo and T. Erneux, "Enhanced performances of a photonic reservoir computer based on a single delayed quantum cascade laser," *Opt. Lett.* **44**(1), 49–52 (2019).
25. Y. S. Hou, G. Q. Xia, E. Jayaprasath, D. Z. Yue, W. Y. Yang, and Z. M. Wu, "Prediction and classification performance of reservoir computing system using mutually delay-coupled semiconductor lasers," *Opt. Commun.* **433**(15), 215–220 (2019).
26. S. Ortín and L. Pesquera, "Reservoir computing with an ensemble of time-delay reservoirs," *Cognit. Comput.* **9**(3), 327–336 (2017).
27. L. Keuninecx, J. Danckaert, and G. Van der Sande, "Real-time audio processing with a cascade of discrete-time delay line-based reservoir computers," *Cognit. Comput.* **9**(3), 315–326 (2017).
28. F. Koyama, "Recent advances of VCSEL photonics," *J. Lightwave Technol.* **24**(12), 4502–4513 (2006).
29. R. Michalzik, *VCSELs: Fundamentals, Technology and Applications of Vertical-Cavity Surface-Emitting Lasers* (Springer-Verlag, 2013).
30. S. Y. Xiang, W. Pan, B. Luo, L. S. Yan, X. H. Zou, and N. Q. Li, "Influence of variable-polarization optical feedback on polarization switching properties of mutually coupled VCSELs," *IEEE J. Sel. Top. Quantum Electron.* **19**(4), 1700108 (2013).
31. H. Zhang, S. Xiang, Y. Zhang, and X. Guo, "Complexity-enhanced polarization-resolved chaos in a ring network of mutually coupled vertical-cavity surface-emitting lasers with multiple delays," *Appl. Opt.* **56**(24), 6728–6734 (2017).
32. N. Jiang, W. Pan, B. Luo, S. Y. Xiang, and L. Yang, "Bidirectional dual-channel communication based on polarization-division-multiplexed chaos synchronization in mutually coupled VCSELs," *IEEE Photonics Technol. Lett.* **24**(13), 1094–1096 (2012).
33. T. Deng, J. Robertson, and A. Hurtado, "Controlled propagation of spiking dynamics in vertical-cavity surface-emitting lasers: towards neuromorphic photonic networks," *IEEE J. Sel. Top. Quantum Electron.* **23**(6), 1800408 (2017).
34. N. Li, H. Susanto, B. R. Cerny, I. D. Henning, and M. J. Adams, "Stability and bifurcation analysis of spin-polarized vertical-cavity surface-emitting lasers," *Phys. Rev. A (Coll. Park)* **96**(1), 013840 (2017).
35. T. Deng, J. Robertson, Z. Wu, G. Xia, X. Lin, X. Tang, Z. Wang, and A. Hurtado, "Stable propagation of inhibited spiking dynamics in vertical-cavity surface-emitting lasers for neuromorphic photonic networks," *IEEE Access* **6**, 67951–67958 (2018).
36. J. Martin-Regalado, F. Prati, M. San Miguel, and N. B. Abraham, "Polarization properties of vertical-cavity surface-emitting lasers," *IEEE J. Quantum Electron.* **33**(5), 765–783 (1997).
37. C. Masoller and N. B. Abraham, "Low-frequency fluctuations in vertical-cavity surface-emitting semiconductor lasers with optical feedback," *Phys. Rev. A* **59**(4), 3021–3031 (1999).
38. R. M. Nguimdo, G. Verschaffelt, J. Danckaert, and G. Van der Sande, "Fast photonic information processing using semiconductor lasers with delayed optical feedback: role of phase dynamics," *Opt. Express* **22**(7), 8672–8686 (2014).
39. A. S. Weigend and N. A. Gershenfeld, "Time series prediction: Forecasting the future and understanding the past," <http://www-psych.stanford.edu/~andreas/Time-Series/SantaFe.html> (1993).

40. K. Hicke, M. A. Escalona-Morán, D. Brunner, M. C. Soriano, I. Fischer, and C. R. Mirasso, "Information processing using transient dynamics of semiconductor lasers subject to delayed feedback," *IEEE J. Sel. Top. Quantum Electron.* **19**(4), 1501610 (2013).
41. A. Hurtado, D. Labukhin, I. D. Henning, and M. J. Adams, "Injection locking bandwidth in 1550-nm VCSELs subject to parallel and orthogonal optical injection," *IEEE J. Sel. Top. Quantum Electron.* **15**(3), 585–593 (2009).